

ARTICLE

DOI: 10.1038/s41467-017-00245-9

OPEN

Gap-state engineering of visible-light-active ferroelectrics for photovoltaic applications

Hiroki Matsuo^{1,3}, Yuji Noguchi^{id}² & Masaru Miyayama^{id}²

Photoferroelectrics offer unique opportunities to explore light energy conversion based on their polarization-driven carrier separation and above-bandgap voltages. The problem associated with the wide bandgap of ferroelectric oxides, i.e., the vanishingly small photoresponse under visible light, has been overcome partly by bandgap tuning, but the narrowing of the bandgap is, in principle, accompanied by a substantial loss of ferroelectric polarization. In this article, we report an approach, ‘gap-state’ engineering, to produce photoferroelectrics, in which defect states within the bandgap act as a scaffold for photogeneration. Our first-principles calculations and single-domain thin-film experiments of BiFeO₃ demonstrate that gap states half-filled with electrons can enhance not only photocurrents but also photovoltages over a broad photon-energy range that is different from intermediate bands in present semiconductor-based solar cells. Our approach opens a promising route to the material design of visible-light-active ferroelectrics without sacrificing spontaneous polarization.

¹Department of Advanced Interdisciplinary Studies, School of Engineering, The University of Tokyo, Tokyo 113-8656, Japan. ²Department of Applied Chemistry, School of Engineering, The University of Tokyo, Tokyo 113-8656, Japan. ³Present address: Department of Chemical System Engineering, School of Engineering, The University of Tokyo, Tokyo 113-8656, Japan. Correspondence and requests for materials should be addressed to Y.N. (email: ynoguchi@fmat.t.u-tokyo.ac.jp)

Innovative strategies have recently been introduced into photovoltaics for efficient solar energy conversion^{1–4}. To absorb light over a broad spectral range and convert the incident energy into electricity, intermediate band (IB) solar cells are designed in which the IB provides electronic states that are partially filled with electrons within the bandgap of a host semiconductor. The IB acts as a stepping stone to generate an electron–hole pair under illumination with below bandgap energy, thereby delivering a large photocurrent^{5–7}. In spite of extensive studies on IB solar cells, the present devices suffer from a reduction in open-circuit voltage compared with the reference cells without IBs⁸.

The photovoltaic (PV) effect in polar materials^{9–11} has allowed researchers to develop novel methods of light energy conversion, generating voltages beyond the bandgap limit of semiconductor p–n junctions^{12, 13}. Because ferroelectrics have multiple polar states¹⁴ that can be selectively stabilized by electric and/or stress fields and exhibit a photoresponse arising from spatial inversion symmetry breaking^{15, 16}, advanced functionalities based on the coupling between the PV effect and the switchable polarization^{17, 18} have stimulated renewed interest in photoferroelectrics^{19, 20}.

The ferroelectric PV effect has been extensively studied for LiNbO₃^{9, 21, 22}, BaTiO₃^{23–27}, PbTiO₃-based perovskites^{28–30} and BiFeO₃ (BFO)^{12, 13, 31, 32}. Recent studies have demonstrated that control of domain architecture can enhance the photoresponse due to the domain-wall-driven effect^{12, 27}. However, these conventional ferroelectrics suffer from poor absorption of visible light because of their bandgap energy (E_g) of $\sim 3–4$ eV^{33–35}. Even for BFO with its relatively small E_g of 2.7 eV^{36, 37}, photons with wavelengths of $\lambda > 460$ nm, constituting > 80 % of the sunlight, cannot be utilized, raising the question of how to activate the PV effect under visible light.

In ferroelectric oxides, their electronic structure with a wide bandgap is characterized by an O-2*p*-derived valence band (VB) and a transition metal (TM)-*d*-derived conduction band (CB) that are accompanied by the orbital interactions of cations and

oxygen atoms^{38, 39}. The TM-*d* and O-2*p* hybridization is enhanced upon atomic displacements⁴⁰, and the hybridization of Pb- or Bi-6*s*(*p*) with O-2*p* induces strong covalent bonding associated with polar lattice distortions^{14, 41}. Both of these cation–oxygen interactions favour coherent off-centre displacements of the cations in their oxygen polyhedra, delivering substantially large spontaneous polarization (P_s)⁴².

Considerable effort has been devoted to narrowing the bandgap of ferroelectrics by rational modification of their compositions. Bandgap tuning has produced narrow-bandgap materials such as KBiFe₂O₅⁴³ with FeO₄ tetrahedra, site-specific LaCoO₃-substituted Bi₄Ti₃O₁₂⁴⁴, heavily Co- and Fe-doped Bi_{3.25}La_{0.75}Ti₃O₁₂⁴⁵, KNbO₃-based solid solution of [KNbO₃]_{1–*x*}[BaNi_{0.5}Nb_{0.5}O_{3– δ}]_{*x*}⁴⁶, and cation-ordered Bi(Fe,Cr)O₃⁴⁷, exhibiting enhanced PV responses under visible light. This bandgap tuning is based on a solid solution or structural formation composed of wide-gap ferroelectrics and non-polar counterparts and is, in principle, accompanied by a substantial reduction in P_s . Meanwhile, the strongly distorted polar lattice yields a robust photoresponse^{15, 16}, called the bulk PV (BPV) effect^{9–11}, and the high photovoltages relies on the large magnitude of P_s . The tradeoff between narrow gap and large polarization motivates us to explore an alternative route to the material design of photoferroelectrics that exhibit a response to low-energy light without sacrificing P_s .

Here, we report an approach, ‘gap-state’ engineering, to produce visible-light-active ferroelectrics. Our approach is based on the creation of defect states within the bandgap, i.e., gap states, half of which are filled with electrons. Under illumination with below-bandgap energy, photon absorption via the half-filled states enables the empty states to receive electrons from the VB and the filled states to supply them to the CB, generating electron–hole pairs. We choose BFO as a model material to investigate the impact on the BPV effect. Our theoretical and experimental investigations demonstrate that the gap states enhance both photocurrents and photovoltages over a broad

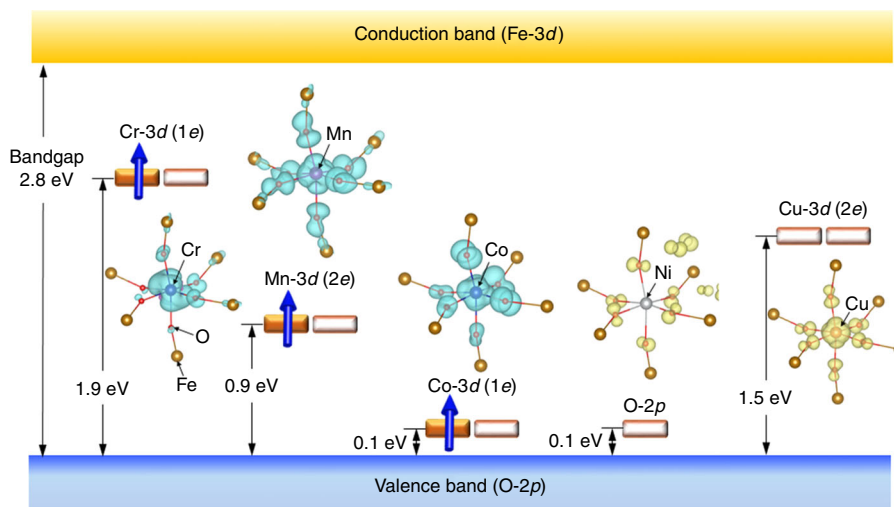


Fig. 1 Wave functions and schematic electronic structures of transition metal (TM=Cr, Mn, Co, Ni and Cu)-doped BFO obtained from DFT calculations. The bandgap (E_g) of BiFeO₃ (BFO) is calculated to be 2.8 eV. The valence band maximum (VBM) is primarily formed by O-2*p*, and the conduction band minimum (CBM) is formed by Fe-3*d*. Filled and open rectangles indicate electron-filled and electron-unoccupied states, respectively. The *e* states of Cr, Mn and Co are half-filled with electrons, while the *e* state of Cu is empty. The blue arrows designate spin-polarized electrons in the gap states. Except for TM=Ni, the gap states are derived from the 3*d* orbitals of TMs hybridized with the surrounding O-2*p*. For TM=Ni, the 3*d*-derived filled states are present below the VBM, and the unoccupied O-2*p* state appears just above the VBM, showing Ni²⁺ with a ligand hole in the O-2*p* state (see text). The wave functions of each gap state are visualized. The wave functions coloured in blue feature orbitals filled with electrons, and those in yellow present empty orbitals, where the iso-surface level remains constant for displaying the wave functions. The 3*d* orbitals of TMs are hybridized with the O-2*p* of the surroundings in different manners reflecting their interactions. The 1*e* state of TM=Cr and Co shows π^+ bonding having d_{xy} and $d_{x^2-y^2}$ characters, while the 2*e* state of TM=Mn and Cu exhibits σ^+ bonding featuring d_{yz} and d_{zx} characters

spectral range. This approach opens a promising route to the development of visible-light-active ferroelectrics with little or no loss of P_s .

Results

Electronic structure calculations. Figure 1 shows the schematic band structures of the TM-doped BFO. The E_g of BFO is calculated to be 2.8 eV, consistent with experiments (2.7 eV^{36,37}). The TM doping does not change significantly in either the E_g or in the electronic character of the VB maximum (VBM) constructed by the O-2p orbitals and the CB minimum (CBM) formed by the Fe-3d orbitals (Supplementary Fig. 1).

According to group theory, the 3d orbitals of the TMs in rhombohedral BFO (C_{3v} symmetry) are split into a_1 , $1e$ and $2e$, where $1e$ and $2e$ denote lower-lying and higher-lying e states, respectively. As shown in Fig. 1, the TMs of Cr, Mn, Co and Cu produce e states within the bandgap. Especially, Cr, Mn and Co yield the gap states, half of which are filled with electrons (half-filled). Relative to the VBM, the gap state is located at 1.9 eV for Cr and 0.9 eV for Mn, while that of Co is in the vicinity of the VBM.

Figure 2 displays the detailed electronic structure of Mn (6%)-doped BFO with the optimized structure, the density of states and the band structure. A partial density of states analysis reveals that

the gap state arises from the hybridized orbital of the Mn-2e and the adjacent O-2p with a significant contribution of Fe-3d, as shown in its wave function (Fig. 1). The 2e state is composed of the d_{yz} - and d_{zx} -derived orbitals (Fig. 2c) and their spin-polarized electron occupancies are in the range of 0.4–0.6 over the entire Brillouin zone. We can therefore regard the 2e as a half-filled state (see Supplementary Note 2).

We found that Ni on the Fe site has a d^8 electron configuration, representing the Ni^{2+} valence state. The d -derived state of Ni^{2+} does not construct a gap state, while an unoccupied O-2p state appears just above the VBM. This result indicates that one hole is transferred from Ni to the ligand oxygen in the NiO_6 octahedron, as reported in ref. 48. This electronic state is expressed as $Ni^{2+}\bar{L}(d^8\bar{L})$, where \bar{L} denotes a ligand hole.

Under illumination with $h\nu$ (photon energy) $>E_g$, photons pump electrons from the VB to the CB and generate electron–hole pairs that are spatially separated in the polar lattice. The optical transition associated with this charge separation delivers a PV current. Given that electronic states within the bandgap, so-called ‘gap’ states, are present, the absorption of light at $h\nu < E_g$ is capable of inducing a PV response. For gap states filled with electrons, pumping electrons from the gap states to the CB injects carriers leaving behind empty traps, and the continuous illumination yields a PV current arising from a sequential trapping and detrapping of photo-generated electrons^{21,22,49}. When gap states are empty, pumping electrons from the VB to the gap states creates holes, and this illumination also brings a PV current via trapping and detrapping of photo-generated holes²⁶.

Provided that the gap states are partially filled with electrons, we expect that the absorption of two sub-bandgap photons generates electron–hole pairs by pumping electrons from the VB to the CB via the gap states, as is seen for IB solar cells^{3,8}. This two-photon absorption has a high probability when its state is half-filled⁵⁰. Moreover, its energy level is preferred in or near the middle of the bandgap. Compared with the filled or empty gap states, where the majority photocarrier is either electron or hole, respectively, we anticipate that the half-filled mid-gap state acts as a scaffold for a robust PV response under illumination with below-bandgap light.

The material design strategy described above leads us to hypothesize that the TMs of Cr and Mn are promising candidates for enhancing the PV effect. Because of a small solubility limit of Cr (several percentage⁵¹), we think that Mn is attractive as the TM dopant for two reasons: there is practically no solubility limit, and its doping does not deteriorate P_s up to 50%⁵². Here, we choose Mn as a dopant for testing the hypothesis of the half-filled gap state and, for comparison, Ni as an example of how the empty state plays a role in the BPV effect.

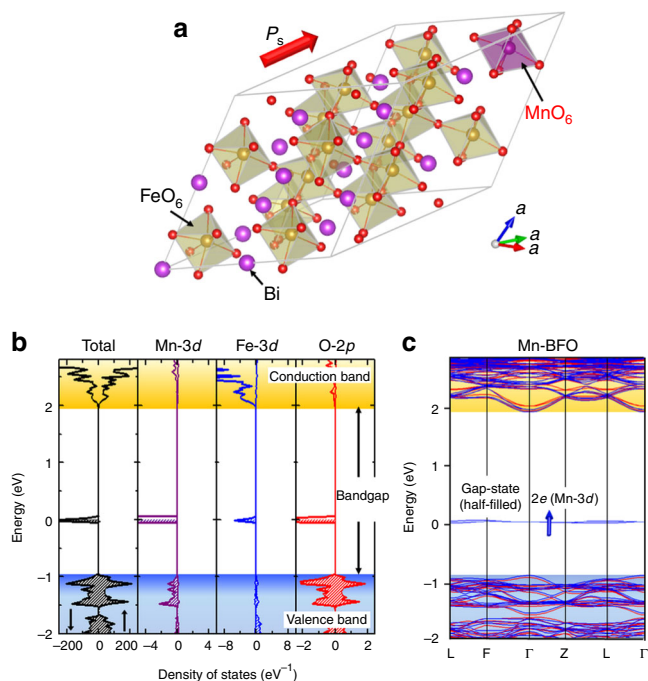


Fig. 2 Crystal and electronic structures of Mn-doped BFO. **a** Optimized crystal structure of Mn-doped BFO [$Bi_{16}(Fe_{15}Mn)O_{48}$] in rhombohedral $R3$ symmetry, **b** total density of states (DOS) and partial DOS (PDOS) of Mn-3d, Fe-3d and O-2p and **c** electronic band structure. In **b**, the nearest neighbour Fe and O atoms of Mn are selected, and majority- and minority-spin bands are described in the right (\uparrow) and left (\downarrow) panels, respectively. The Mn-3d orbitals are split into up-spin a_1 , $1e$ and down-spin a_1 , $1e$ and $2e$. Taking the d^4 electron configuration of Mn^{3+} into account, we can regard it as up-spin $a_1^1, 1e^2$ and $2e^1$ and down-spin $a_1^0, 1e^0$ and $2e^0$. In **c**, red and blue lines represent majority- and minority-spin states, respectively, and the blue arrow indicates a spin-polarized electron in the gap state, exhibiting that Mn provides the half-filled gap (2e) state. For the 2e state, the d_{yz} - and d_{zx} -derived orbitals are degenerate at the Γ and Z points in the Brillouin zone, while the degeneracy is lifted once the k -point is away from these high-symmetry points; its energy difference is 0.03 eV at the L point

Photocurrent properties. In Fig. 3a, we illustrate the single-domain (SD) structure associated with the pseudocubic $[hkl]$ directions showing the crystallographic orientations (also see Supplementary Fig. 2). For a precise description of the 4° vicinal angle from the pseudocubic axes owing to the miscut of the substrate, we employ the lab-coordinate (xyz) system exhibiting the PV measurement configuration (Fig. 3b). Figure 3c presents the J - V_{bias} properties in the y direction under illumination ($h\nu = 2.4$ eV) at $\omega = 90^\circ$ (ω denotes light polarization angle). The Mn-BFO film shows a V_y of -3.1 V and a J_y of $-15 \mu A cm^{-2}$ that are much higher than those of the BFO film ($V_y = -0.6$ V, $J_y = -1.3 \mu A cm^{-2}$).

In Fig. 3d, e, we exhibit the J_y and J_{-x} data, respectively, as a function of ω at $h\nu = 2.4$ eV for the Mn-BFO film. We found that J_{-x} (Fig. 3e) shows a sinusoidal dependence on ω without offset,

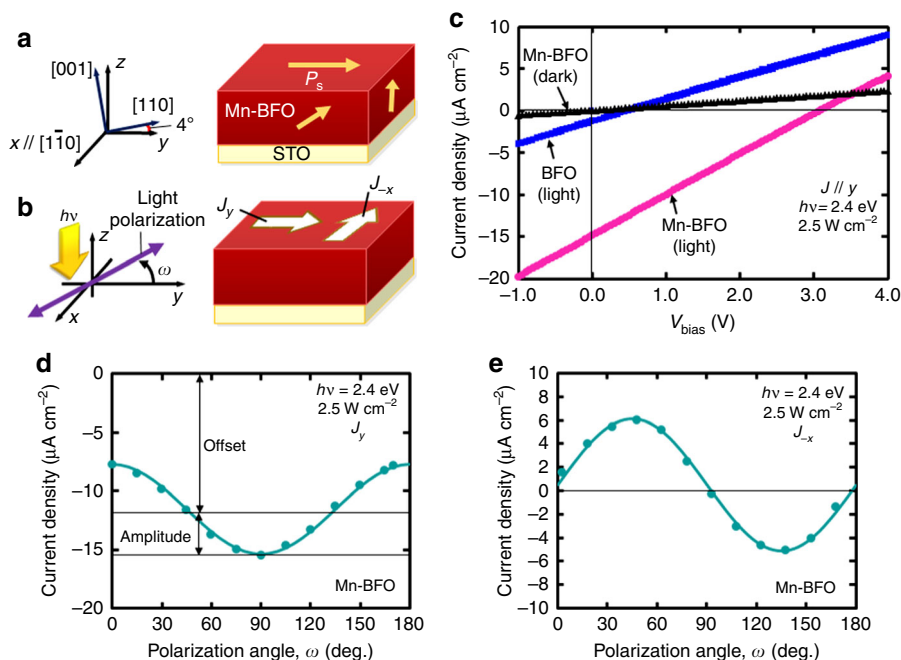


Fig. 3 Measurement configuration and photovoltaic (PV) properties of the Mn-BFO film. **a** Schematic of the single-domain (SD) structure associated with the pseudocubic $[hkl]$ directions exhibiting the crystallographic orientations with respect to the lab-coordinate (xyz) system. The x axis lies along $[1\bar{1}0]$, and the y and z axes are 4° away from $[110]$ and $[001]$, respectively. **b** PV measurement configuration in which polarized light with photon energy $h\nu$ propagates along the z axis and is incident on the sample surface. The incident light has a polarization angle (ω) from the y axis in the xy plane. The short-circuit current density (J_{sc}) and open-circuit voltage (V_{oc}) along the m direction are expressed as J_m and V_m , respectively. A positive J_m indicates that the photocurrent flows in the m direction. The bias voltage (V_{bias}) at which the current density (J) becomes zero is denoted by $-V_m$. **c** Current density–bias voltage (J – V_{bias}) properties along the y direction under dark and illuminated ($h\nu=2.4$ eV) conditions, where the polarization angle ω is aligned so that the PV response becomes maximum for both the BFO and Mn-BFO (Mn 5%) films. Light polarization angle ω dependences of short-circuit currents **d** J_y , and **e** J_{-x} in the Mn-BFO film

while J_y (Fig. 3d) has an offset of $J_{y,off}$ in addition to a sinusoidal oscillation with an amplitude $J_{y,amp}$. (the data of the BFO film are presented in Supplementary Fig. 4c, d). Even at $h\nu=1.9$ eV, the Mn-BFO film clearly shows similar sinusoidal behaviour in J_y and J_{-x} (Supplementary Fig. 5c, d, whereas we cannot observe a PV response for the BFO film.

Photon energy dependence. In Fig. 4a, b, we show the $h\nu$ dependences of $|V_y|$ and $|J_y|$, respectively. Under illumination at $h\nu=3.1$ eV, the BFO film generates a $|V_y|$ of 4.3 V. However, $|V_y|$ decreases to 0.6 V at $h\nu=2.4$ eV and below the detection limit at $h\nu=1.9$ eV (Fig. 4a). A similar reduction in $|J_y|$ is also detected in the low- $h\nu$ range (Fig. 4b). We note that both the $|V_y|$ and $|J_y|$ of the Mn-BFO film are much larger than those of the BFO film at $h\nu$ above E_g in addition to below E_g . The Mn-BFO film exhibits a $|V_y|$ exceeding the bandgap voltage under illumination at $h\nu=2.4$ eV. The Mn-BFO film clearly exhibits a substantial PV response at 1.9 eV and no detectable signal at 1.5 eV (Supplementary Fig. 11). The overall tendency of the PV response with respect to $h\nu$ agrees qualitatively with the results of the absorption spectra (Supplementary Fig. 3). (An estimation procedure of α is presented in Supplementary Note 4 and Supplementary Fig. 10.)

The Ni-BFO film displays a relatively high $|J_y|$ whereas the $|V_y|$ is lower than 0.1 V at 2.4 eV (Supplementary Fig. 8). The small $|V_y|$ is attributed to its high conductivity (Supplementary Table 3), and the resultant photogenerated power $|J_y \times V_y|/4$ becomes much smaller. We note that its high conductivity and density functional theory (DFT) calculation results of Ni-doped BFO confirm $Ni^{2+}\bar{L}(d^8\bar{L})$ state in the Ni-BFO film (see Supplementary Note 3 and Supplementary Fig. 9).

Discussion

We estimate the BPV tensor elements (β_{15} , β_{22} , β_{31} and β_{33}) from the ω dependences of J_y and J_{-x} by taking into account the 4° deviation of the measurement directions from the pseudocubic axes, the details of which are described in ref. ³². In Fig. 5a, we present the BPV tensor elements at $h\nu=2.4$ eV obtained by fitting the experimental data with the analytic equations. We found that the absolute values of the Mn-BFO film are 2–10 times as large as those of the BFO film. This result clearly demonstrates that the Mn doping dramatically enhances the BPV effect under illumination with below-bandgap light. The apparent ω -dependent photocurrents of the Mn-BFO film at $h\nu=1.9$ eV (Supplementary Fig. 5c, d) enable us to obtain the BPV tensor elements (Supplementary Fig. 7).

Figure 5b exhibits the BPV tensor elements at $h\nu=3.1$ eV in a similar manner. The Mn doping decreases $|\beta_{15}|$ and $|\beta_{31}|$ but increases $|\beta_{33}|$ markedly. This result indicates that the larger values of $|V_y|$ and $|J_y|$ at $h\nu=3.1$ eV achieved by the Mn doping (Fig. 4a, b) originate from the enhanced β_{33} . The BPV tensor elements are listed in Supplementary Table 1.

Here, we discuss why the Mn doping markedly enhances the BPV effect at $h\nu < E_g$. The BFO film shows the BPV effect at $h\nu=3.1$ eV because photons with $h\nu \geq E_g$ (2.7 eV) can generate electron–hole pairs that are subsequently separated in the polar lattice. A small but significant photoresponse of the BFO film at $h\nu=2.4$ eV is attributed to a dipole-forbidden p - d charge transfer transition⁵³.

The robust response of the Mn-BFO film at $h\nu < E_g$ enables us to consider that the optical transitions via the half-filled gap state enhances the BPV effect. The Mn-BFO film at $h\nu=2.4$ eV exhibits the comparable or large BPV tensor elements compared with the

BFO film at $h\nu=3.1$ eV ($h\nu>E_g$), supposing that the PV effect observed at $h\nu=2.4$ eV stems from electron–hole pair generation. The details of the photogenerated carriers are described in Supplementary Note 5. In principle, visible light with $h\nu$ higher than the sub-bandgap energies can create electron–hole pairs via the gap state by the following two-photon absorption. A sub-bandgap transition pumps an electron from the gap state to the CB (a charge transfer from Mn to its adjacent Fe) and does so

from the VB to the gap state (a charge transfer from O to Mn), where these processes are accompanied by the changes in the valence state of Mn. Even when the optical transitions occur successively, electron–hole pairs are generated, because once an electron or hole is pumped the carrier is directed away from Mn in the polar lattice.

The Mn-BFO film exhibits an apparent PV response at $h\nu=1.9$ eV but no detectable short-circuit photocurrent at $h\nu=1.5$ eV (Supplementary Fig. 11). These results combined with the optical transition processes (Supplementary Note 5 and Supplementary Fig. 12) suggest that the majority photocarrier at $h\nu=1.9$ eV is electron–hole pair. In contrast, we found that photogenerated holes can induce the BPV effect in the Ni-BFO film at $h\nu=1.9$ eV (Supplementary Fig. 8). The Ni doping provides the empty state in the vicinity of the VBM. This shallow state gives rise to the high conductivities under dark and illumination (Supplementary Table 3), leading to the high currents with sacrificing the voltages. The much higher photogenerated power of the Mn-BFO film compared with the Ni-BFO film shows that the half-filled gap state is effective for the BPV effect.

Next, we discuss the origin of the enhanced β in Mn-BFO at $h\nu<E_g$. The BPV tensor element β_{ij} can be written as $\beta_{ij}=\alpha G_{ij}$ ²¹, where α denotes the absorption coefficient and G_{ij} indicates the Glass coefficient determined by the shift vector representing the average distance travelled by the coherent carriers during their lifetimes¹⁵. Though anisotropy in α ⁵⁴ may cause variations in the photocurrents, the experimental data of the ω -dependent J_y and J_{-x} are well fitted by the analytical equations adopting an isotropic α , showing that the anisotropy in α does not have a significant influence on our PV results.

One possible origin of the enhancement in β by the Mn doping is an increase in α . We found, however, that the Mn doping yields only a 22% increase in α at $h\nu = 2.4$ eV (Supplementary Fig. 3) while the β of the Mn-BFO film is 2–10 times as large as that of the BFO film, demonstrating that the enhanced β cannot be explained solely by its slightly larger α .

We now estimate G_{ij} representing photogeneration strength in the BPV effect. The one-photon transition of the VB to CB has a contribution of $\beta_{ij,1} (= \alpha_1 G_{ij,1})$ to the BPV effect, as observed for the BFO film. The two-photon absorption via the gap ($2e$) state delivers an additional $\beta_{ij,2} = \alpha_2 G_{ij,2}$ for the Mn-BFO film, where α_1 and α_2 denote their respective absorption coefficients. Because the Mn doping does not change the fundamental feature of the VB and the CB, β_{ij} representing the net BPV response of Mn-BFO

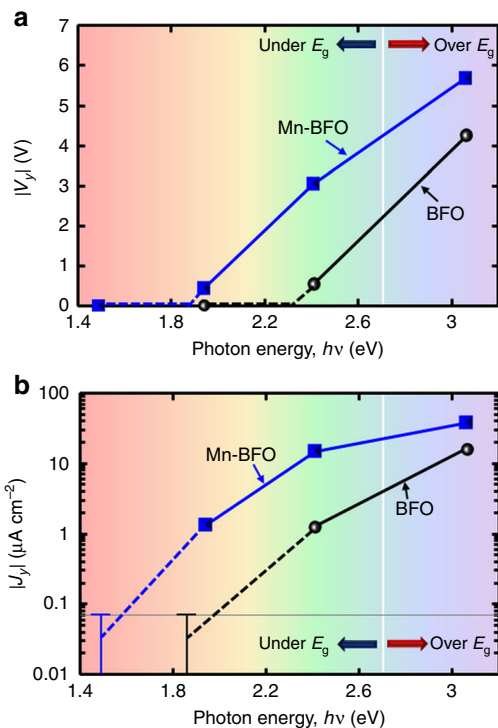


Fig. 4 Photogenerated current and voltage as a function of photon energy ($h\nu$). **a** $|V_y|$ and **b** $|J_y|$, where the polarization angle ω is aligned so that the PV response becomes maximum: $\omega = 90^\circ$ in the BFO film (regardless of $h\nu$); $\omega = 0^\circ$ at $h\nu = 3.1$ eV, and $\omega = 90^\circ$ at $h\nu = 2.4$ eV and 1.9 eV in the Mn-BFO (Mn 5 %) film. The horizontal line in **b** indicates the detection limit in our measurements. The J - V_{bias} properties of the films of BFO ($h\nu=3.1$ eV) and Mn-BFO ($h\nu=3.1$ eV, 1.9 eV and 1.5 eV) in the y direction are shown in Supplementary Fig. 6a, b 11, respectively

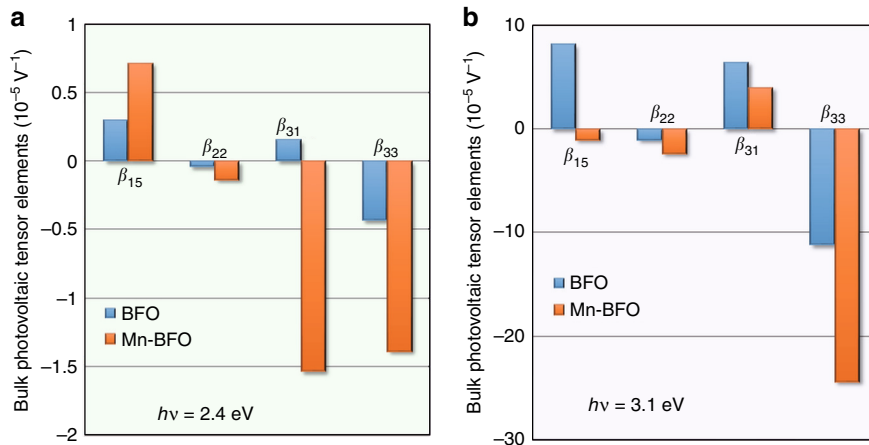


Fig. 5 Bulk photovoltaic (BPV) tensor elements (β_{ij}). Under illumination at **a** $h\nu=2.4$ eV and **b** $h\nu=3.1$ eV estimated from light polarization angle ω dependences of short-circuit currents. The data of the BFO film are shown in Supplementary Fig. 4 and that of the Mn-BFO film are exhibited in Supplementary Fig. 5

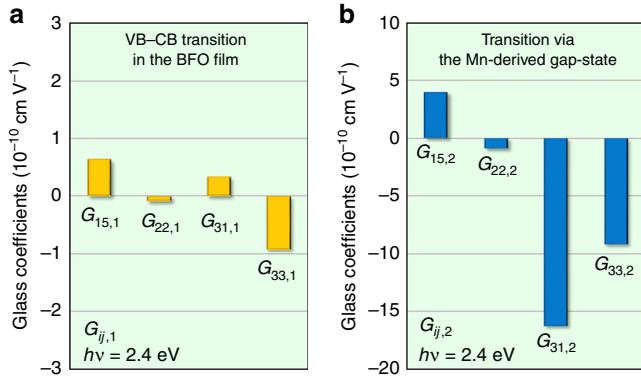


Fig. 6 Glass coefficients of $G_{ij,1}$ and $G_{ij,2}$ at $h\nu=2.4$ eV. **a** $G_{ij,1}$ represents the photogenerated strength arising from the one-photon optical transition of the VB to the CB in the BFO film, while **b** $G_{ij,2}$ reflects what is attributed to the charge transfer transition via the Mn-3d-derived gap (2e) state

is expressed as $\beta_{ij} = \beta_{ij,1} + \beta_{ij,2}$. As a result, $G_{ij,2}$ arising from the Mn-derived gap state can be expressed as

$$G_{ij,2} = \frac{\beta_{ij,2}}{\alpha_2} = \frac{1}{\alpha_2} \left(\beta_{ij}^{\text{Mn-BFO}} - \beta_{ij}^{\text{BFO}} \right), \quad (1)$$

where β_{ij}^{BFO} and $\beta_{ij}^{\text{Mn-BFO}}$ are their respective experimental β_{ij} values.

Using the relations of $\alpha_1 = \alpha^{\text{BFO}}$ and $\alpha_1 + \alpha_2 \approx \alpha^{\text{Mn-BFO}}$ and the experimental result of $\alpha^{\text{Mn-BFO}} = 1.22\alpha^{\text{BFO}}$ ($h\nu=2.4$ eV, see Supplementary Fig. 3), we obtain $\alpha_2 = 0.22\alpha^{\text{BFO}}$. From the experimentally determined β_{ij}^{BFO} and $\beta_{ij}^{\text{Mn-BFO}}$ values (Fig. 5a),

$G_{ij,1}$ ($= \frac{\beta_{ij,1}}{\alpha_1} = \frac{\beta_{ij}^{\text{BFO}}}{\alpha^{\text{BFO}}}$) and $G_{ij,2}$ at $h\nu=2.4$ eV are estimated as displayed in Fig. 6a, b, respectively. The $G_{ij,1}$ and $G_{ij,2}$ values at $h\nu=3.1$ eV, 2.4 eV and 1.9 eV are summarized in Supplementary Table 2, where the data at 3.1 eV and 1.9 eV are estimated in a similar manner at 2.4 eV. The above estimation reveals that $|G_{ij,2}|$ is much larger than $|G_{ij,1}|$: $|G_{31,2}|$ is ~ 50 times as large as $|G_{31,1}|$ at $h\nu=2.4$ eV. These results lead to the conclusion that the major origin of the enhanced PV response achieved by the Mn doping is not the increase in α but the large Glass coefficients.

Finally, we address how the half-filled gap states in ferroelectrics are different from IBs in semiconductor solar cells. For bulk IB solar cells, such as $\text{V}_2\text{In}_{14}\text{S}_{24}$ ⁵⁵ and $\text{ZnTe}:\text{O}$ [7], extended IBs are situated in or near the middle of the bandgap. The IBs act as a stepping stone for generating electron-hole pairs by absorbing sub-bandgap photons and thereby photocurrents are enhanced by an increase in α at $h\nu < E_g$ ⁸. The crucial problem to be overcome is a reduction in V_{oc} with respect to the reference cells without IBs at room temperature⁸, where the Shockley-Read-Hall (SRH) recombination⁵⁶ influences their V_{oc} to some extent. In contrast, the gap-state engineering in ferroelectrics can not only increase α but also enhance V_{oc} . In fact, the Mn doping leads to larger values of both V_{oc} and J_{sc} (Fig. 4). Although the SRH recombination is suggested to reduce the carrier lifetimes, the gap state increases the Glass coefficients by over one order of magnitude at $h\nu=2.4$ eV ($h\nu < E_g$). This experimental fact shows that the average drift velocity of photo-generated electrons and holes is higher in the presence of the gap state, and thereby delivering the robust BPV effect.

Our experimental and theoretical investigations demonstrate that the mid-gap half-filled state acts as a scaffold for the BPV effect over a broad $h\nu$ range. Gap-state engineering is revealed to enhance not only photocurrents but also photovoltages, and therefore providing a promising route to the material design of visible-light-active photoferroelectrics.

Methods

DFT calculations. First-principles calculations based on DFT⁵⁷ were performed within the generalized gradient approximation (GGA)⁵⁸ in the projector-augmented-wave method⁵⁹, as implemented in the Vienna *ab initio* simulation package⁶⁰. We employed the gradient corrected exchange-correlation functional of the PBEsol (Perdew-Burke-Ernzerhof revised for solids)⁶¹ for structural optimization. To obtain insight into the role of the defect states arising from TM elements, accurate information on bandgaps is an essential foundation for investigating their influence on the bulk PV effect. We therefore adopted the density functional MBJLDA (modified Becke-Johnson exchange plus local density approximation)⁶² to calculate the electronic band structures and density of states. Within the simplified GGA+*U* approach⁶³, on-site Coulomb interaction parameters of $U-J=4$ eV were added to all the *d* elements of the TMs, including Fe. The Monkhorst-Pack *k*-point mesh of $3 \times 3 \times 3$ was adopted for the supercell of $\text{Bi}_{16}(\text{Fe}_{15}\text{TM})\text{O}_{48}$ in rhombohedral *R3* symmetry (TM=Cr, Mn, Co, Ni and Cu) (see Supplementary Note 1). All results were obtained by explicitly treating 15 valence electrons for Bi ($5d^{10}6s^26p^3$), 8 for Fe ($3d^64s^2$), 6 for Cr ($3d^44s^2$), 7 for Mn ($3d^54s^2$), 9 for Co ($3d^74s^2$), 10 for Ni ($3d^84s^2$), 11 for Cu ($3d^{10}4s^1$) and 6 for O ($2s^22p^4$). The plane-wave cutoff energy was set at 520 eV, and the electronic energy was converged to less than 10^{-5} eV in all calculations.

Film fabrication and characterization. Thin films of BFO, Mn (5%)-doped BFO (Mn-BFO) and Ni (5%)-doped BFO (Ni-BFO) with a thickness of 300 nm were deposited on vicinal SrTiO_3 (STO) (100) single-crystal substrates with a miscut angle of 4° along the [110] direction by pulsed-laser deposition with a KrF excimer laser ($\lambda=248$ nm). We set the following parameters for the film preparation: a substrate temperature of 630 °C, an oxygen pressure of 11 Pa, a laser energy of 1.2 J cm^{-2} and a laser repetition rate of 7 Hz. Domain structures were investigated by piezoresponse force microscopy (PFM) and X-ray diffraction measurements. For the PFM observations, in-plane and out-of-plane phase and amplitude images were measured.

PV measurements. The PV properties of the SD films along the *y* and $-x$ directions were measured under illumination with light at wavelengths of 405 nm ($h\nu=3.1$ eV), 515 nm ($h\nu=2.4$ eV) and 639 nm ($h\nu=1.9$ eV). The light propagated along the *z* axis and was incident on the sample surface. The power of the incident light was set at 2.5 W cm^{-2} . The incident light was adjusted to have a polarization angle (ω) from the *y* axis in the *xy* plane using a polarizing plate and a half-wave plate. Pseudocubic notation is adopted throughout this article to express the crystallographic directions.

The BPV tensor elements (β_{15} , β_{22} , β_{31} and β_{33}) were estimated from the ω dependences of J_y and J_{-x} . When linearly polarized light is incident on a ferroelectric crystal, the photocurrent density \mathbf{J} derived from the BPV effect is expressed by the equation

$$\mathbf{J}_i = I_{\text{opt}} \beta_{ijk} \mathbf{e}_j \mathbf{e}_k, \quad (2)$$

where β_{ijk} is a third-rank BPV tensor, I_{opt} is the incident light intensity, and \mathbf{e}_j and \mathbf{e}_k are the components of the unit vectors along the *j* and *k* directions in the crystallographic coordinate system, respectively. For ferroelectrics in C_{3v} symmetry, β_{ijk} in matrix notation is expressed as

$$\beta_{ijk} = \begin{pmatrix} 0 & 0 & 0 & 0 & \beta_{15} & -\beta_{22} \\ -\beta_{22} & \beta_{22} & 0 & \beta_{15} & 0 & 0 \\ \beta_{31} & \beta_{31} & \beta_{33} & 0 & 0 & 0 \end{pmatrix}. \quad (3)$$

We obtain $J_{[110]}$ and $J_{[\bar{1}10]}$ as follows:

$$J_{[110]} = \frac{I_{\text{opt}}}{3\sqrt{3}} (\sqrt{2}\beta_{15} + \beta_{22} + 2\sqrt{2}\beta_{31} + \sqrt{2}\beta_{33}) + \frac{I_{\text{opt}}}{3\sqrt{3}} (\sqrt{2}\beta_{15} - 2\beta_{22} - \sqrt{2}\beta_{31} + \sqrt{2}\beta_{33}) \sin[2(\omega + \frac{\pi}{4})]. \quad (4)$$

$$J_{[\bar{1}10]} = I_{\text{opt}} \left[\frac{2}{\sqrt{6}}\beta_{15} + \frac{1}{\sqrt{3}}\beta_{22} \right] \sin(2\omega) \quad (5)$$

When we neglect the deviation of the measurement directions from the crystallographic orientations and the decay of light in the ferroelectric layer by absorption, we can regard $J_{[110]}$ as J_y and $J_{[\bar{1}10]}$ as J_{-x} . The details of the accurate descriptions of J_y and J_{-x} taking into account the light absorption and the vicinal angle are described in ref. 32. For the calculations of the PV tensor elements, we adopted the relation $\beta_{22}=1/10\beta_{33}$ that has been proven for LiNbO_3 in C_{3v} symmetry.

Data Availability. The data that support the findings of this study are available from the corresponding author on reasonable request.

Received: 8 February 2017 Accepted: 12 June 2017

Published online: 08 August 2017

References

- Lee, M. M., Teuscher, J., Miyasaka, T., Murakami, T. N. & Snaith, H. J. Efficient hybrid solar cells based on meso-superstructured organometal halide perovskites. *Science* **338**, 643–647 (2012).
- Liu, M., Johnston, M. B. & Snaith, H. J. Efficient planar heterojunction perovskite solar cells by vapour deposition. *Nature* **501**, 395–398 (2013).
- Martí, A., Cuadra, L., Luque, A. in *Proc. 28th IEEE Photovoltaics Specialists Conf.* 904–943 (IEEE, 2000).
- Luque, A. et al. General equivalent circuit for intermediate band devices: Potentials, currents and electroluminescence. *J. Appl. Phys.* **96**, 903–909 (2004).
- Linares, P. G. et al. Voltage recovery in intermediate band solar cells. *Sol. Energy Mater. Sol. Cells* **98**, 240–244 (2012).
- Lucena, R., Aguilera, I., Palacios, P., Wahnón, P. & Conesa, J. C. Synthesis and spectral properties of nanocrystalline V-substituted In_2S_3 , a novel material for more efficient use of solar radiation. *Chem. Mater.* **20**, 5125–5127 (2008).
- Wang, W., Lin, A. S. & Phillips, J. D. Intermediate-band photovoltaic solar cell based on ZnTe:O. *Appl. Phys. Lett.* **95**, 11103 (2009).
- Luque, A., Martí, A. & Stanley, C. Understanding intermediate-band solar cells. *Nat. Photonics* **6**, 146–152 (2012).
- Glass, A. M. High-voltage bulk photovoltaic effect and the photorefractive process in LiNbO_3 . *Appl. Phys. Lett.* **25**, 233–235 (1974).
- Fridkin, V. M. & Popov, B. N. Anomalous photovoltaic effect in ferroelectrics. *Sov. Phys. Uspekhi* **21**, 981–991 (1978).
- Dalba, G., Soldo, Y., Rocca, F., Fridkin, V. M. & Sainctavit, P. Giant bulk photovoltaic effect under linearly polarized x-ray synchrotron radiation. *Phys. Rev. Lett.* **74**, 988–991 (1995).
- Yang, S. Y. et al. Above-bandgap voltages from ferroelectric photovoltaic devices. *Nat. Nanotechnol.* **5**, 143–147 (2010).
- Bhatnagar, A., Roy Chaudhuri, A., Heon Kim, Y., Hesse, D. & Alexe, M. Role of domain walls in the abnormal photovoltaic effect in BiFeO_3 . *Nat. Commun.* **4**, 2835 (2013).
- Cohen, R. E. Origin of ferroelectricity in perovskite oxides. *Nature* **358**, 136–138 (1992).
- Young, S. M. & Rappe, A. M. First principles calculation of the shift current photovoltaic effect in ferroelectrics. *Phys. Rev. Lett.* **109**, 116601 (2012).
- Young, S. M., Zheng, F. & Rappe, A. M. First-principles calculation of the bulk photovoltaic effect in bismuth ferrite. *Phys. Rev. Lett.* **109**, 236601 (2012).
- Choi, T., Lee, S., Choi, Y. J., Kiryukhin, V. & Cheong, S.-W. Switchable ferroelectric diode and photovoltaic effect in BiFeO_3 . *Science* **324**, 63–66 (2009).
- Lee, D. et al. Polarity control of carrier injection at ferroelectric/metal interfaces for electrically switchable diode and photovoltaic effects. *Phys. Rev. B* **84**, 125305 (2011).
- Fridkin, V. M. *Photoferroelectrics* (Springer Berlin Heidelberg, 1979).
- Kreisel, J., Alexe, M. & Thomas, P. A. A photoferroelectric material is more than the sum of its parts. *Nat. Mater.* **11**, 260 (2012).
- Festl, H. G., Hertel, P., Krätzig, E. & von Baltz, R. Investigations of the photovoltaic tensor in doped LiNbO_3 . *Phys. Status Solidi* **113**, 157–164 (1982).
- Inoue, R. et al. Enhanced photovoltaic currents in strained Fe-doped LiNbO_3 films. *Phys. Status Solidi Appl. Mater. Sci.* **212**, 2968–2974 (2015).
- Koch, W. T. H., Munser, R., Ruppel, W. & Würfel, P. Bulk photovoltaic effect in BaTiO_3 . *Solid State Commun.* **17**, 847–850 (1975).
- Koch, W. T. H., Munser, R., Ruppel, W. & Würfel, P. Anomalous photovoltage in BaTiO_3 . *Ferroelectrics* **13**, 305–307 (1976).
- Zenkevich, A. et al. Giant bulk photovoltaic effect in thin ferroelectric BaTiO_3 films. *Phys. Rev. B* **90**, 161409 (2014).
- Inoue, R. et al. Photocurrent characteristics of Mn-doped barium titanate ferroelectric single crystals. *Jpn. J. Appl. Phys.* **52**, 09KF03 (2013).
- Inoue, R. et al. Giant photovoltaic effect of ferroelectric domain walls in perovskite single crystals. *Sci. Rep.* **5**, 14741 (2015).
- Uchino, K., Miyazawa, Y. & Nomura, S. High-voltage photovoltaic effect in PbTiO_3 -based ceramics. *Jpn. J. Appl. Phys.* **21**, 1671–1674 (1982).
- Qin, M., Yao, K. & Liang, Y. C. High efficient photovoltaics in nanoscaled ferroelectric thin films. *Appl. Phys. Lett.* **93**, 122904 (2008).
- Kholkin, A., Boiarkine, O. & Setter, N. Transient photocurrents in lead zirconate titanate thin films. *Appl. Phys. Lett.* **72**, 130–132 (1998).
- Nakashima, S. et al. Bulk photovoltaic effect in a BiFeO_3 thin film on a SrTiO_3 substrate. *Jpn. J. Appl. Phys.* **53**, 09PA16 (2014).
- Matsuo, H. et al. Bulk and domain-wall effects in ferroelectric photovoltaics. *Phys. Rev. B* **94**, 214111 (2016).
- Dhar, A. & Mansingh, A. Optical properties of reduced lithium niobate single crystals. *J. Appl. Phys.* **68**, 5804–5809 (1990).
- Moret, M. P., Devillers, M. A. C., Wörhoff, K. & Larsen, P. K. Optical properties of PbTiO_3 , $\text{PbZr}_x\text{Ti}_{1-x}\text{O}_3$, PbZrO_3 films deposited by metalorganic chemical vapor on SrTiO_3 . *J. Appl. Phys.* **92**, 468–474 (2002).
- Panda, B., Dhar, A., Nigam, D., Bhattacharya, D. & Ray, K. Optical properties of RF sputtered strontium substituted barium titanate thin films. *Thin Solid Films* **332**, 46–49 (1998).
- Ihlefeld, J. F. et al. Optical band gap of BiFeO_3 grown by molecular-beam epitaxy. *Appl. Phys. Lett.* **92**, 142908 (2008).
- Basu, S. R. et al. Photoconductivity in BiFeO_3 thin films. *Appl. Phys. Lett.* **92**, 091905 (2008).
- Piskunov, S., Heifets, E., Eglitis, R. I. & Borstel, G. Bulk properties and electronic structure of SrTiO_3 , BaTiO_3 , PbTiO_3 perovskites: an *ab initio* HF/DFT study. *Comput. Mater. Sci.* **29**, 165–178 (2004).
- Resta, R., Posternak, M. & Baldereschi, A. Towards a quantum theory of polarization in ferroelectrics: the case of KNbO_3 . *Phys. Rev. Lett.* **70**, 1010–1013 (1993).
- Filippetti, A. & Hill, N. A. Coexistence of magnetism and ferroelectricity in perovskites. *Phys. Rev. B* **65**, 195120 (2002).
- Cohen, R. E. & Krakauer, H. Electronic structure studies of the differences in ferroelectric behavior of BaTiO_3 and PbTiO_3 . *Ferroelectrics* **136**, 65–83 (1992).
- Kuroiwa, Y. et al. Evidence for Pb-O covalency in tetragonal PbTiO_3 . *Phys. Rev. Lett.* **87**, 217601 (2001).
- Zhang, G. et al. New high T_C multiferroics KBiFe_2O_5 with narrow band gap and promising photovoltaic effect. *Sci. Rep.* **3**, 1265 (2013).
- Choi, W. S. et al. Wide bandgap tunability in complex transition metal oxides by site-specific substitution. *Nat. Commun.* **3**, 689 (2012).
- An, H. et al. Large enhancement of the photovoltaic effect in ferroelectric complex oxides through bandgap reduction. *Sci. Rep.* **6**, 28313 (2016).
- Grinberg, I. et al. Perovskite oxides for visible-light-absorbing ferroelectric and photovoltaic materials. *Nature* **503**, 509–512 (2013).
- Nechache, R. et al. Bandgap tuning of multiferroic oxide solar cells. *Nat. Photonics* **61**, 61–67 (2015).
- Mizokawa, T. et al. Electronic structure of PrNiO_3 studied by photoemission and x-ray-absorption spectroscopy: band gap and orbital ordering. *Phys. Rev. B* **52**, 13865–13873 (1995).
- Noguchi, Y., Inoue, R. & Miyayama, M. Electronic origin of defect states in Fe-doped LiNbO_3 ferroelectrics. *Adv. Condens. Matter Phys.* **2016**, 2943173 (2016).
- Martí, A., Cuadra, L. & Luque, A. Partial filling of a quantum dot intermediate band for solar cells. *IEEE Trans. Electron Devices* **48**, 2394–2399 (2001).
- Kim, J., Kim, S., Choi, E. & Kim, W. Enhanced ferroelectric properties of Cr-doped BiFeO_3 thin films prepared by chemical solution deposition. *Appl. Phys. Lett.* **88**, 132901 (2006).
- Matsuo, H., Kitanaka, Y., Inoue, R., Noguchi, Y. & Miyayama, M. Heavy Mn-doping effect on spontaneous polarization in ferroelectric BiFeO_3 thin films. *Jpn. J. Appl. Phys.* **54**, 10NA03 (2015).
- Pisarev, R. V., Moskvina, A. S., Kalashnikova, A. M. & Rasing, T. Charge transfer transitions in multiferroic BiFeO_3 and related insulators. *Phys. Rev. B* **79**, 235128 (2009).
- Choi, S. G. et al. Optical anisotropy and charge-transfer transition energies in BiFeO_3 from 1.0 to 5.5 eV. *Phys. Rev. B* **83**, 100101 (2011).
- Palacios, P., Aguilera, I., Sánchez, K., Conesa, J. C. & Wahnón, P. Transition-metal-substituted indium thiopinsels as novel intermediate-band materials: prediction and understanding of their electronic properties. *Phys. Rev. Lett.* **101**, 046403 (2008).
- Shockley, W. & Read, W. T. Statistics of the recombination of holes and electrons. *Phys. Rev.* **87**, 835–842 (1952).
- Kohn, W. & Sham, L. J. Self-consistent equations including exchange and correlation effects. *Phys. Rev.* **140**, A1133–A1138 (1965).
- Perdew, J. P., Burke, K. & Ernzerhof, M. Generalized gradient approximation made simple. *Phys. Rev. Lett.* **77**, 3865 (1996).
- Blöchl, P. E. Projector augmented-wave method. *Phys. Rev. B* **50**, 17953–17979 (1994).
- Kresse, G. & Hafner, J. Ab initio molecular-dynamics simulation of the liquid-metal-amorphous-semiconductor transition in germanium. *Phys. Rev. B* **49**, 14251–14269 (1994).
- Perdew, J. P. et al. Restoring the density-gradient expansion for exchange in solids and surfaces. *Phys. Rev. Lett.* **100**, 136406 (2008).
- Tran, F. & Blaha, P. Accurate band gaps of semiconductors and insulators with a semilocal exchange-correlation potential. *Phys. Rev. Lett.* **102**, 226401 (2009).
- Anisimov, V. I., Zaanen, J. & Andersen, O. K. Band theory and Mott insulators: Hubbard U instead of Stoner I. *Phys. Rev. B* **44**, 943–954 (1991).

Acknowledgements

This research is supported by JSPS through a Grant-in-Aid for JSPS Fellows (14J04693), partly by JSPS KAKENHI Grant Number 26249094. We thank T. Numata (HORIBA Techno Service Co., Ltd) for photoluminescence measurements and K. Yoshida for

assistance with PV measurements. We acknowledge R. Inoue and Y. Kitanaka for fruitful discussion.

Author contributions

H.M. and Y.N. conceived and designed the experiments. H.M. performed the experiments and the tensor analyses. Y.N. calculated the electronic structures. H.M., Y.N. and M.M. wrote the paper.

Additional information

Supplementary Information accompanies this paper at doi:10.1038/s41467-017-00245-9.

Competing interests: The authors declare no competing financial interests.

Reprints and permission information is available online at <http://npg.nature.com/reprintsandpermissions/>

Publisher's note: Springer Nature remains neutral with regard to jurisdictional claims in published maps and institutional affiliations.



Open Access This article is licensed under a Creative Commons Attribution 4.0 International License, which permits use, sharing, adaptation, distribution and reproduction in any medium or format, as long as you give appropriate credit to the original author(s) and the source, provide a link to the Creative Commons license, and indicate if changes were made. The images or other third party material in this article are included in the article's Creative Commons license, unless indicated otherwise in a credit line to the material. If material is not included in the article's Creative Commons license and your intended use is not permitted by statutory regulation or exceeds the permitted use, you will need to obtain permission directly from the copyright holder. To view a copy of this license, visit <http://creativecommons.org/licenses/by/4.0/>.

© The Author(s) 2017